Reciprocal carrier collection in organic photovoltaics

C. Kyle Renshaw,[1,*] Cody W. Schlenker,[2,*] Mark E. Thompson,[2] and Stephen R. Forrest[1]

[1]*Department of Electrical Engineering and Computer Science, Physics, and Materials Science and Engineering, University of Michigan, Ann Arbor, Michigan 48109 USA*

[2]*Department of Chemistry and Center for Energy Nanoscience, University of Southern California, Los Angeles, California 90089 USA*

(Received 14 May 2011; published 18 July 2011)

Buffer layers between the acceptor and cathode can perform several functions in organic photovoltaic devices, such as providing exciton blocking, protection of active layers against damage from cathode deposition, and optical spacing to maximize the electric field in the active device region. Here, we study electron collection by replacing the common buffer layer, bathocuproine, with a series of six, substituted *tris*(β-diketonato)Ru(III) analogues in the structure: indium-tin-oxide/copper phthalocyanine/C_{60}/buffer/Ag. These buffer layers enable collection of photogenerated electrons by transporting holes from the cathode to the C_{60}/buffer interface, followed by recombination with photogenerated electrons in the acceptor. We use a model for free-polaron and polaron-pair dynamics to describe device operation and the observed inflection in the current-voltage characteristics. The device characteristics are understood in terms of hole transfer from the highest occupied molecular orbital energy levels of several Ru-complexes to the acceptor.

DOI: 10.1103/PhysRevB.84.045315 PACS number(s): 88.40.jr, 84.60.Jt, 71.35.−y, 73.50.−h

I. INTRODUCTION

Buffer layers are frequently employed between the acceptor and cathode in organic photovoltaic (OPV) devices to improve their power conversion efficiencies (PCE). The layer typically has multiple functions, including as (i) an exciton blocker that prevents quenching at the acceptor-cathode (A/C) interface,[1,2] (ii) a spacer to optimize the optical field at the active donor-acceptor (D/A) junction,[3–5] and (iii) a physical buffer to protect the acceptor layer from damage incurred during cathode deposition.[6,7] A commonly used buffer material, bathocuproine (BCP),[2] is effective at suppressing parasitic exciton quenching and protecting the active layers,[7] but its ability to act as an optical spacer is limited due to the thicknesses that can be used. That is, charge transport in this and similar wide energy gap materials depends on introducing charge-conducting pathways through traps induced by damage incurred during cathode metal deposition. Typically, this damage extends only 5–10 nm from the buffer layer surface. This thickness, however, is insufficient to use the layer as an optimal optical spacer that can concentrate the incident field at the active D/A interface.[5,8,9]

Recently, a more thickness-tolerant buffer material, *tris*(acetylacetonato)ruthenium(III) ($Ru(acac)_3$), was shown to efficiently transport holes along its highest occupied molecular orbital (HOMO) energy level directly to the acceptor and, hence, does not depend on the presence of a high density of trap states for conduction.[10] Here, $Ru(acac)_3$ is a ground-state neutral metal complex with a low-spin d^5 open shell,[11] leading to efficient hole transport. Figure 1(a) depicts the carrier transport mechanism in $Ru(acac)_3$ buffers. Holes are injected from the cathode to the HOMO of the buffer and then transported to the acceptor-buffer (A/B) interface. Recombination of photogenerated electrons in the lowest unoccupied molecular orbital (LUMO) of the acceptor occurs across the A/B interface with the positive charge in the buffer HOMO.

In this study, a series of *tris*(β-diketonato)ruthenium(III) analogues bearing various aromatic and electron withdrawing substituents are used as buffer materials in OPV devices. We analyze their current density vs. voltage (J-V) characteristics based on a model employing geminate polaron-pair (PP) and carrier dynamics.[12] The buffer forms a Type-II heterojunction (HJ)[10] with the C_{60} acceptor as shown in Fig. 1(b), resulting in two antipolar diodes with the first (forward) diode formed by the donor-acceptor (D/A) junction and the second (reverse) diode formed by the A/B junction. This arrangement results in an inflection in the J-V characteristics, which is commonly observed in OPVs with nonideal cathode contacts.[13,14] In previous studies, this behavior has been attributed to a reverse-biased diode that inhibits charge collection at one of the contacts[15,16] and has been treated phenomenologically using an equivalent circuit model consisting of two opposing diodes.[17,18] Here the inflection is found to be a fundamental property depending on the energy levels of the buffer, and is related to a reduced polaron pair (PP) recombination rate at the A/B interface. That is, the A/B junction forms a bottleneck for charge extraction when PP recombination is slow compared to dissociation into free polarons.

We use ultraviolet photoemission spectroscopy (UPS) to measure the energy levels at the A/B and buffer/cathode interfaces, supporting our conclusion that PP recombination at the A/B interface can lead to a divergence from the ideal exponential J-V characteristics of a single-junction device.[12] We find that buffer materials yielding the most pronounced inflection have a deeper HOMO level corresponding to a larger A/B interface energy gap (defined as the difference in the LUMO energy of the acceptor and the HOMO energy of the buffer, viz.: $\Delta E_{\mathrm{HL}} = E_{\mathrm{LUMO},A} - E_{\mathrm{HOMO},B}$) and a smaller PP recombination rate. The reduction in PP recombination with an increase in ΔE_{HL} suggests that electron transfer between the acceptor and buffer occurs via Marcus transfer in the inverted regime.[19] This indicates that charge extraction and, consequently, the PCE for reciprocal junction devices can be optimized by tuning ΔE_{HL}. The model developed to quantitatively describe the inflected J-V characteristics is based on the formalism developed previously by Giebink *et al.*[12] and,

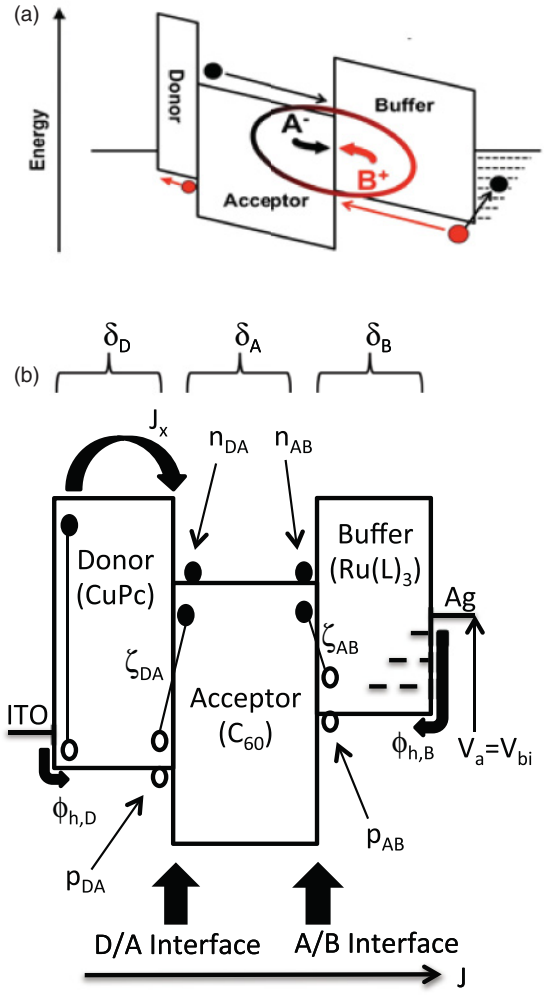

FIG. 1. (Color online) (a) Schematic of the reciprocal carrier collection process. (b) Diagram of the model for reciprocal carrier collection. Exciton flux J_x reaches the donor/acceptor interface (D/A) and creates polaron pairs (PPs) at density $\zeta_{\rm DA}$. These PPs are in dynamic equilibrium with electrons with density $n_{\rm DA}$ in the acceptor LUMO and holes with density $p_{\rm DA}$ in the donor HOMO. Similarly, at the reciprocal acceptor/buffer interface (A/B), there are PPs (density $\zeta_{\rm AB}$) and carriers $n_{\rm AB}$ and $p_{\rm AB}$ in the acceptor LUMO and buffer HOMO, respectively. The interfaces are coupled by $n_{\rm DA}$ and $n_{\rm AB}$ via current density (J) continuity and whose magnitudes are determined by the voltage drop across the acceptor $\delta_A(V_a\text{-}V_{\rm bi})$. Similarly, $p_{\rm DA}$ and $p_{\rm AB}$ are determined by respective density of states, injection barriers ($\phi_{h,D}$ and $\phi_{h,B}$), and voltage drops (δ_D and δ_B).

hence, can be generally applied to a range of organic junctions that exhibit reciprocal behavior.

This paper is organized as follows: In Sec. II, we discuss the theory describing the current in double heterojunctions characteristic of Ru-complex-based buffers used in OPVs. The model is based on exciton, charge, and PP dynamics; in Sec. III we describe the experimental methods for materials synthesis, device fabrication, and measurement; in Sec. IV we provide experimental results; in Sec. V we fit the experimental data to the model presented in Sec. II and discuss the physical processes that limit the power conversion efficiency in OPVs; and in Sec. VI, we present conclusions.

II. THEORY

Giebink *et al.* have proposed a description of the J-V characteristics of organic (i.e., excitonic) D/A junctions[12] that balances PP generation, dissociation, and recombination at the interface with free polarons injected from or collected at the contacts. In that model, excitons with flux, J_x, diffuse to the D/A interface where the bound states are dissociated into PPs. The PPs subsequently recombine to the ground state at a rate, $k_{r,\rm DA}$, or dissociate to form free polarons at a rate, $k_{d,\rm DA}$. Free polarons at the interface (corresponding to a hole density in the donor, $p_{\rm DA}$, and an electron density in the acceptor, $n_{\rm DA}$) can recombine by a Langevin process to form PPs at a rate $k_{\rm rec}$. Here, we assume that there are occupied traps in the donor and acceptor and that bimolecular recombination is dominated by free polarons recombining with trapped polarons at the interface.[12] This occurs at a rate $k_{{\rm rec},n}$ when free polarons in the acceptor recombine with trapped polarons in the donor, $p_{{\rm DA},t}$, and $k_{{\rm rec},p}$ when free polarons in the donor recombine with trapped polarons in the acceptor, $n_{{\rm DA},t}$. The PP density, ζ, is then obtained from:

$$\begin{aligned} &J_x/a_{\rm DA} - k_{r,\rm DA}(\zeta-\zeta_0) - k_{d,\rm DA}\zeta + k_{{\rm rec},n} n_{\rm DA} p_{{\rm DA},t} \\ &\quad + k_{{\rm rec},p} n_{{\rm DA},t} p_{\rm DA} = 0, \\ &k_{d,\rm DA}\zeta - k_{{\rm rec},n} n_{\rm DA} p_{{\rm DA},t} - k_{{\rm rec},p} n_{{\rm DA},t} p_{\rm DA} + J/q a_{\rm DA} = 0, \end{aligned} \tag{1}$$

where the first equation describes the steady-state PP density, and the second gives the balance of charge, also in steady-state. Here, q is the electronic charge, $a_{\rm DA}$ is the width of the D/A junction defined by the spatial extent of interacting PPs, $\zeta_0 = k_{{\rm rec},n} n_{{\rm DA},0} p_{{\rm DA},t,0}/k_{d,{\rm DA},0} + k_{{\rm rec},p} n_{{\rm DA},t,0} p_{{\rm DA},0}/k_{d,{\rm DA},0}$ is the equilibrium PP density, and $k_{d,{\rm DA},0}$ is the equilibrium PP dissociation efficiency. Also, $n_{{\rm DA},0}, n_{{\rm DA},t,0}, p_{{\rm DA},0}$, and $p_{{\rm DA},t,0}$ are the equilibrium free and trapped electron and hole densities at the interface. Important variables used are defined in Table I.

In quasi-equilibrium, the interface polaron densities are related to the charge densities at the contact and the injection barrier following:

$$\begin{aligned} n_{\rm DA} &= n_{\rm cathode} \exp\left(\frac{\delta_A q(V_a - V_{\rm bi})}{k_B T}\right) \\ &\approx N_{\rm LUMO} \exp\left(-\frac{\phi_e}{k_B T}\right) \exp\left(\frac{\delta_A q(V_a - V_{\rm bi})}{k_B T}\right), \end{aligned} \tag{2}$$

with a similar expression for holes.[20] Here, T is the temperature, k_B is Boltzmann's constant, $n_{\rm cathode}$ is the carrier density at the cathode, $N_{\rm LUMO}$ is the density of LUMO states in the acceptor, ϕ_e is the electron injection barrier at the contact, δ_A is the fraction of the applied voltage, V_a, dropped across the acceptor layer, and $V_{\rm bi}$ is the built-in voltage given by the difference in the anode and cathode work functions. Now, the trapped electron distribution in organic materials is commonly described by an exponential function:

$$n_t \approx H_A \exp\left(\frac{E_{\rm Fn} - E_{\rm LUMO}}{k_B T_{t,A}}\right) \approx H_A \left(\frac{n}{N_{\rm LUMO}}\right)^{1/l_A}, \tag{3}$$

TABLE I. Definition of variables.

Variable		Definition	Units
D/A	A/B	Junction variables	
J_x	0	Exciton current density reaching D/A HJ	$cm^{-2}\ s^{-1}$
ζ	ζ_{AB}	Polaron pair density at HJ	cm^{-3}
a_{DA}	a_{AB}	Polaron pair spatial extent	cm
$k_{rec,n}$, $k_{rec,p}$	$k_{rec,AB}$	Free carrier bimolecular recombination coefficient	$cm^{-3}\ s^{-1}$
$k_{d,DA}$	$k_{d,AB}$	Polaron pair dissociation rate	s^{-1}
$k_{r,DA}$	$k_{r,AB}$	Polaron pair recombination rate	s^{-1}
$\eta_{d,DA}$	$\eta_{d,AB}$	Polaron pair dissociation efficiency	
n_{DA}, p_{DA}	n_{AB}, p_{AB}	Free electron and hole densities at the HJ	cm^{-3}
$n_{DA,t}$, $p_{DA,t}$	$n_{AB,t}$, $p_{AB,t}$	Trapped electron and hole densities at the HJ	cm^{-3}
J_{sD}, J_{sA}	J_{sAB}	Saturation current density of HJ	$A\ cm^{-2}$
n_D, n_A	1	Ideality factors due to trap limited recombination	
		Layer Variables	
δ_D, δ_A, δ_B		Fractions of potential dropped across donor, acceptor and buffer layers	
$N_{HOMO,D}$, N_{LUMO}, $N_{HOMO,B}$		Donor HOMO, acceptor LUMO and buffer HOMO densities of states	cm^{-3}
H_D, H_A		Band edge trap densities in the donor and acceptor	cm^{-3}
l_D, l_A		Characteristic temperature ratio for hole and electron trap distributions in the donor and acceptor	
p_{anode}		Density of holes in the donor at the anode	cm^{-3}
ϕ_D, ϕ_B		Hole injection barrier into the donor and buffer	eV
ΔE_{HL}		Interface energy gap at A/B HJ	eV

with a similar expression for trapped holes. Here, H_A is the total trap density, $T_{t,A}$ is the characteristic trap temperature, and $l_A = T/T_{t,A}$. Then, Giebink *et al.* derive the following expression for the current density-voltage characteristics of a D/A junction in the presence of traps:

$$J = J_{sD}\left(\exp\left(\frac{qV_a}{n_D k_B T}\right) - \frac{k_{d,DA}}{k_{d,DA,0}}\right) + J_{sA}\left(\exp\left(\frac{qV_a}{n_A k_B T}\right) - \frac{k_{d,DA}}{k_{d,DA,0}}\right) - q\eta_{d,DA}J_x. \quad (4)$$

with ideality factors $n_{D(A)} = l_{D(A)}/(\delta_{A(D)}(l_{D(A)} - 1) + 1)$.

The saturation currents, J_{sD} and J_{sA}, are defined as in Ref. 12, $\eta_{d,DA} = k_{d,DA}/(k_{d,DA} + k_{r,DA})$ is the PP dissociation efficiency, and $n_{D(A)}$ is the ideality factor of the recombination processes characteristic of the donor (acceptor) layer.

To apply this model to the case of reciprocal carrier collection as found in Ru-complex (or RuL_3, where L = ligand) buffers, we use a similar approach for both the D/A and A/B interfaces [c.f., (2)] by considering the polaron states as shown in Fig. 1(b). The A/B junction is a reverse-biased diode with respect to the D/A junction, and the two are coupled by current continuity in the acceptor layer. Hence, we write the following to describe polaron recombination at the A/B interface, which is coupled to similar expressions at the D/A junction:

$$\begin{aligned} -k_{r,AB}(\zeta_{AB} - \zeta_{AB,0}) - k_{d,AB}\ \zeta_{AB} + k_{rec,AB}n_{AB}p_{AB} &= 0 \\ k_{d,AB}\ \zeta_{AB} - k_{rec,AB}n_{AB}p_{AB} - J/qa_{AB} &= 0. \end{aligned} \quad (5)$$

We have neglected exciton flux as a source of PP generation since the optical field near the contact is small, minimizing exciton generation near this second interface.[1] To further simplify the model, we ignore the presence of traps in the buffer. Traps at this interface could be accounted for in the same manner as at the D/A interface; however, we find that we can accurately fit the *J-V* characteristics by assuming a trap-free junction. Continuity requires that polarons leaving the D/A junction must build up at the A/B interface.

We can solve for polaron, ζ_{AB}, and interface electron densities using (5). As in Ref. 12, quasi-equilibrium for holes at the A/B interface gives the current-dependent interfacial electron density, n_{AB}:

$$n_{AB} = \left(\frac{k_{d,AB}}{k_{d,AB,0}} - \frac{J}{J_{sAB}}\right)n_{AB,0}\exp\left(\frac{\delta_B q V_a}{k_B T}\right)$$

where

$$J_{sAB} = qa_{AB}(1 - \eta_{d,AB})k_{rec,AB}n_{AB,0}p_{AB,0}. \quad (6)$$

From the voltage drop across the acceptor δ_A, we can relate the electron densities n_{AB} and n_{DA} via:

$$n_{DA} = n_{AB}\ \exp\left(\frac{\delta_A q(V_a - V_{bi})}{k_B T}\right). \quad (7)$$

The solution to the double junction then is given by (12) in Ref. 12 for the D/A junction, and by using Eqs. (2), (6), and (7) to evaluate both the free and trapped electron densities in the layers. Thus:

$$J = J_{sD}\left(\left(\frac{k_{d,AB}}{k_{d,AB,0}} - \frac{J}{J_{sAB}}\right)\exp\left(\frac{qV_a}{n_D k_B T}\right) - \frac{k_{d,DA}}{k_{d,DA,0}}\right) + J_{sA}\left(\left(\frac{k_{d,AB}}{k_{d,AB,0}} - \frac{J}{J_{sAB}}\right)^{1/l_A} \times \exp\left(\frac{qV_a}{n_A k_B T}\right) - \frac{k_{d,DA}}{k_{d,DA,0}}\right) - q\eta_{d,DA}J_x,$$

with

$$J_{sD} = qa_{\mathrm{DA}}(1-\eta_{d,\mathrm{DA}})k_{\mathrm{rec},n}n_{\mathrm{AB},0}H_D\left(\frac{p_{\mathrm{anode}}}{N_{\mathrm{HOMO},D}}\right)^{1/l_D} \times \exp\left(-\frac{\alpha_D}{k_BT}\right)$$
$$J_{sA} = qa_{\mathrm{DA}}(1-\eta_{d,\mathrm{DA}})k_{\mathrm{rec},p}p_{\mathrm{anode}}H_A\left(\frac{n_{\mathrm{AB},0}}{N_{\mathrm{LUMO}}}\right)^{1/l_A} \times \exp\left(-\frac{\alpha_A}{k_BT}\right). \quad (8)$$

The corresponding ideality factors are given by:

$$n_D = l_D/(l_D-\delta_D(l_D-1)),$$
$$n_A = l_A/(l_A-(\delta_A+\delta_B)(l_A-1)),$$
$$\alpha_D = (1-n_D\delta_B)qV_{\mathrm{bi}}/n_D,$$
$$\alpha_A = (1-n_A\delta_B/l_A)qV_{\mathrm{bi}}/n_A. \quad (9)$$

The performance of OPVs with reciprocal carrier collection are fully described by Eqs. (8) and (9). Note that these expressions are analogous to those for a single junction but differ primarily in the current-dependent prefactors that result from the dependence of n_{DA} on n_{AB} (i.e., on current continuity). Also, $\alpha_{\mathrm{D(A)}}$ and $n_{\mathrm{D(A)}}$ differ slightly from their definitions for a single junction but have a similar dependence on trap temperature, interface energy gap, and voltage distributions δ_{D}, δ_{A}, and δ_{B}. The exponent of the second current term in Eq. (8) precludes an analytical expression for J.

To elucidate the dominant features leading to reciprocal carrier collection, it is useful to simplify Eq. (8). For example, one of the diode terms can be neglected when the J-V characteristics are dominated by a single recombination process, i.e., free electrons in the acceptor recombining with trapped holes in the donor, or free holes in the donor with trapped electrons in the acceptor. Indeed, monopolar recombination is consistent with the analysis of CuPc/C_{60} junctions at room temperature.[12] To be general, we keep the second term of Eq. (8) based on free holes recombining with trapped electrons by letting $J_{sD}\to 0$, but find that fitting this nonanalytic equation to our device data yields a trap temperature ratio of $l_A = 0.99 \pm 0.01$. This suggests that recombination occurs via free electrons with trapped holes. In this case, we keep J_{sD}, and set $J_{sA}\to 0$, linearizing the right-hand side of Eq. (8). Additionally, for $V_a < \mathrm{V_{bi}}$, where the A/B junction is forward-biased, we retain the zero-field dissociation rate for the A/B junction, $k_{d,\mathrm{AB}} \approx k_{d,\mathrm{AB},0}$. Equation (8) is thereby simplified to:

$$J = \left(J_{sD}\left(\exp\left(\frac{qV_A}{n_Dk_BT}\right)-\frac{k_{d,\mathrm{DA}}}{k_{d,\mathrm{DA},0}}\right)-J_{\mathrm{ph}}\right)\Big/ \times\left(1+\frac{J_{sD}}{J_{s\mathrm{AB}}}\exp\left(\frac{qV_a}{n_Dk_BT}\right)\right), \quad (10)$$

where the photocurrent density is $J_{\mathrm{ph}} = q\eta_{d,\mathrm{DA}}J_x$.

In Fig. 2 we plot characteristic curves predicted by Eq. (10) for several values of $J_{s\mathrm{AB}}$, where we assume $k_{d,\mathrm{DA}} = k_{d,\mathrm{DA},0}$ for simplicity. The simulations show that the characteristic "opposing diode" behavior is increasingly apparent at decreasing reverse-diode saturation currents. Furthermore, current saturation occurs in both forward and reverse bias, as rectification of either the D/A and A/D junction correspondingly limits the total current. The magnitude of the inflection depends on the ratio of J_{sD} to $J_{s\mathrm{AB}}$. The current behaves like a single diode with ideality factor, n_D when $J_{s\mathrm{AB}} \gg J_{sD}$, or as antipolar diodes with a J-V inflection as $J_{s\mathrm{AB}} \to J_{sD}$.

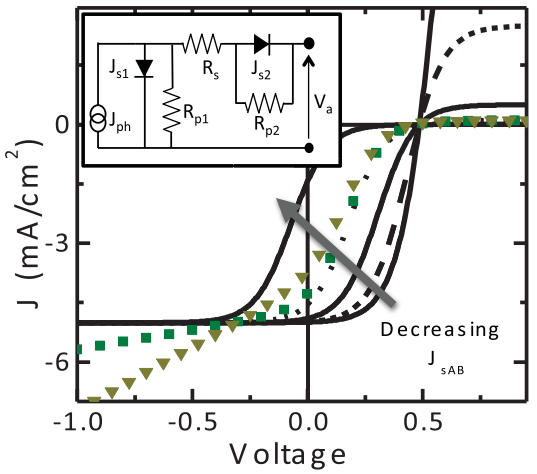

FIG. 2. (Color online) Characteristic current density-voltage (J-V) curves calculated from the model in text re-create the inflection behavior seen in OPV devices with a charge extraction barrier. For these calculations, we assume $J_{\mathrm{ph}} = 5$ mA is the photocurrent, and $J_{sD} = 10\ \mu$A and $n = 3$ are the reverse saturation current density and ideality factor of the forward donor/acceptor junction, respectively. Solid and broken lines correspond to different saturation currents of the reversed acceptor/buffer junction spanning $J_{s\mathrm{AB}} = 12.5$, 2.5, 0.5, 0.2, and 0.04 mA/cm^2. Symbols show the reverse bias slope generated by shunt resistances of 300 Ω (triangles) and 1 kΩ (squares) in the equivalent circuit model, shown in the inset.

As noted above, the resulting inflection, or S-shaped kink, in J vs. V near zero bias has been previously qualitatively attributed to a reverse-biased diode at one of the contacts and is typically described by an equivalent circuit model as shown in the Fig. 2 inset.[15,17,18] Both junctions are described by the Shockley equation modified to include a series (R_s) and junction shunt (R_p) resistance. Only the active junction is forward biased and produces photocurrent; the second junction is reverse biased. In this case, we can write the phenomenological pair of equations as

$$J = J_{s1}\left(\exp\left(\frac{qV_1}{n_1k_BT}\right)-1\right)+\frac{V_1}{R_{p1}}-J_{\mathrm{ph}}$$
$$-J = J_{s2}\left(\exp\left(-\frac{qV_2}{n_2k_BT}\right)-1\right)-\frac{V_2}{R_{p2}}. \quad (11)$$

Here, the subscripts 1 and 2 refer to the D/A and A/B junctions, respectively, and the applied voltage is dropped across the two junctions via, $V_a - \mathrm{JR}_s = \mathrm{V}_1 + \mathrm{V}_2$. At low current densities, the effect of R_s is small, and hence is

ignored. When $R_{p2} \gg V_2/J$, then the coupled equations are reduced to

$$J = J_{s1}\left(\left(1-\frac{J}{J_{s2}}\right)^{n_2/n_1}\exp\left(\frac{qV_a}{n_1k_BT}\right)-1\right)+\frac{V_a}{R_{p1}} + \frac{n_2k_BT}{qR_{p1}}\ln\left(1-\frac{J}{J_{s2}}\right)-J_{\rm ph}. \quad (12)$$

Equation (12) has the same form as (8) for a single junction if the shunt current is negligible, i.e., $R_{p1}\to\infty$. Note that the physical origin of the shunt resistance cannot be understood using the equivalent circuit to fit the large reverse bias slope and simulate the commonly observed deviations from the Shockley equation. The effect that parallel resistance has on the reverse bias slope is also shown in Fig. 2 for $R_p = 300\ \Omega$ and 1 k Ω. In contrast, the treatment here and in Ref. 12 attributes the reverse bias slope to the field dependence of the PP recombination rate, as described by Onsager-Braun dissociation.[21]

III. EXPERIMENTAL

Materials. Preparation of the metal complexes employed the following precursors: ruthenium(III) chloride hydrate (99+%); 1,3-dephenyl-1,3-propanedione (98%); 4,4-difluoro-1-phenyl-1,3-butanedione (97%); 4,4,4-trifluoro-1-phenyl-1,3-butanedione (99%); 4,4,4-trifluoro-1-(2-naphthyl)-1,3-butanedione (99%); 4,4,4-trifluoro-1-(2-thienyl)-1,3-butanedione (99%). Various Ru β-diketonate derivatives were synthesized by the "ruthenium blue" method of Endo *et al.*,[22] summarized in Fig. 3(a). Ruthenium trichloride was refluxed in ethanol under N_2. Excess chelating ligand was introduced, and the liberated H^+ was quenched with multiple fractions of bicarbonate. Complexes were purified over an activated alumina (neutral, Alfa Aesar) column with benzene (EMD; 99.92%) as the eluant and recrystallized from ethanol or ethanol/benzene. Ligands were

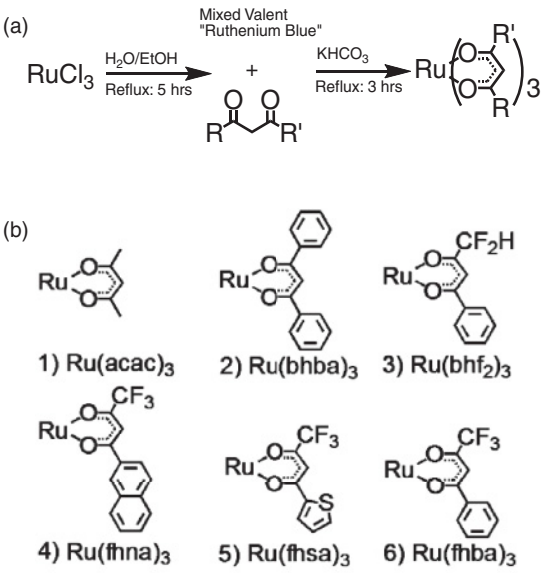

FIG. 3. (a) "Ruthenium Blue" process for synthesizing the Ru-based complexes. (b) Molecular structure of the ligand bonded to the Ru core for each buffer layer. Numbers given to each material are ordered by decreasing voltage at the inflection.

chosen based on their ability to maximize vapor processability, increased intermolecular electronic communication, and the relative HOMO energies of the resulting complex. Depending on the magnitude of the electron withdrawing effects exerted by the β-position substituents[23,24] on the electron density of the chelating oxygen atoms[25] in each ligand, the *d*-orbitals of the metal complexes are progressively stabilized via increasingly electron-deficient chelating atoms. The resulting products were characterized by electron impact ionization mass spectrometry (HP 5973), ultraviolet-visible spectroscopy (Agilent 8453), and solution cyclic voltammetry (EG & G Potentiostat/Galvanostat, Model 283).[26]

Device Fabrication and Characterization. Devices were deposited on glass substrates commercially coated with indium tin oxide (ITO with thickness, 1500 $\pm$ 100 Å; sheet resistance, 20 $\pm$ 5 Ω/sq.; transmission, 84% at a wavelength of λ = 550 nm). Substrates were solvent cleaned and UV-ozone treated for 10 minutes prior to loading into a high vacuum deposition chamber (base pressure $<2\times10^{-6}$ Torr). All ruthenium analogues, copper phthalocyanine (CuPc from Aldrich; 97%), C_{60} (MER; 99+%), and $Ru(acac)_3$ (Aldrich; 97%) were purified via thermal gradient sublimation (base pressure $< 2\times10^{-7}$ Torr). Organic and Ag (Alfa Aesar, 99.9999%) layer thicknesses and deposition rates were monitored by a quartz crystal microbalance to yield OPV devices with the structure: ITO/CuPc(400Å)/C_{60}(400Å)/buffer/Ag(1000Å). The *J-V* measurements were performed using a Keithly 2420 SourceMeter® in the dark and under AM1.5G, 1 kW/m^2 white light illumination from a 300W Xe arc lamp, with total power measured using an NREL-calibrated Si photodiode. Fits to the *J-V* data were performed in Matlab using a nonlinear, least-squares, trust-region algorithm.

UV Photoelectron Spectroscopy. The HOMO energies of the RuL_3 buffer layers on C_{60}/ITO or Ag were measured by UPS. ITO-coated glass substrates with sheet resistance of $< 15\ \Omega$/sq. were solvent cleaned and UV-ozone treated prior to loading into an ultra-high vacuum (UHV) chamber. Prior to the deposition of a 50 Å thick RuL_3 film: (i) 50 Å thick C_{60} films were deposited onto ITO substrates, or (ii) 300 Å thick Ag films were deposited onto *p*-type Si. The organic films were deposited by organic molecular beam deposition (base pressure: 10^{-9} Torr) from Knudsen cells, while the Ag films were deposited in a separate UHV interconnected chamber by thermal evaporation. Thickness was monitored by an ellipsometrically calibrated quartz crystal microbalance. Following deposition, the samples were immediately transferred under UHV ($<1\times10^{-9}$ Torr) to the UPS chamber. Photoelectron spectra were collected using a Thermo VG hemispherical electron energy analyzer with a pass function full-width half maximum of 0.16 eV (calibrated by fitting the Fermi step of a freshly deposited Au film) to filter electrons photoemitted from the sample by a 21.22eV He(I) emission line from a gas-discharge lamp. To minimize sample charging, electrical contact to the ITO film was maintained by a metal clip attached to a copper puck and connected to ground. The sample was biased at -9.00 V to ensure that the low-kinetic-energy electrons pass through the analyzer.

The LUMO energies were estimated by electrochemical methods[27] performed under nitrogen against ferrocene/ferrocenium in dry acetonitrile with tetrabutylammonium

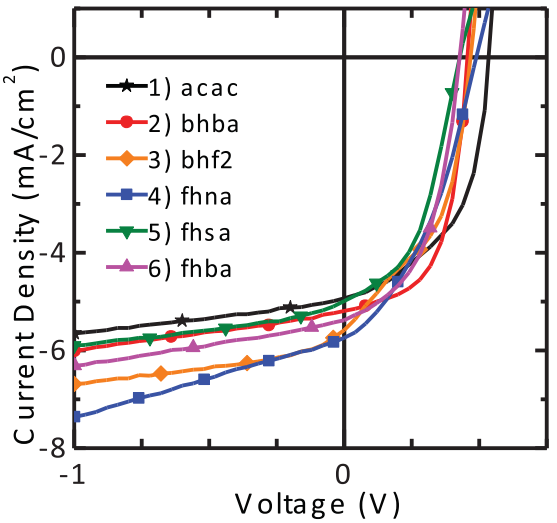

FIG. 4. (Color online) Current density vs. voltage (J-V) characteristics under approximately 1 sun AM1.5G illumination of ITO/copper-phthalocyanine (40 nm)/C_{60} (40 nm)/buffer (10 nm)/Ag (100 nm) devices. Data are shown by symbols and lines. Slight differences in photocurrent magnitude from device to device are attributed to small variations in light intensity and device efficiency.

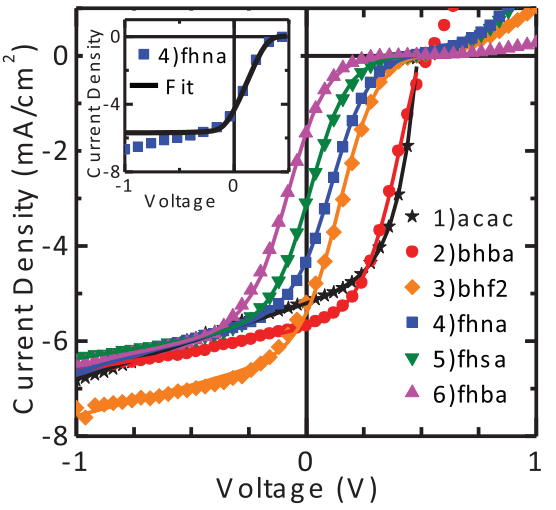

FIG. 5. (Color online) Current density vs. voltage (J-V) characteristics under approximately 1 sun AM1.5G illumination of ITO/copper-phthalocyanine (40 nm)/C_{60} (40 nm)/buffer (20 nm)/Ag (100 nm) devices. Data are shown by symbols, and fits to the model in text up to breakdown at ~0.5 V are shown by solid lines. Inset: Fit (line) of the measured reverse bias characteristic (symbols) ignoring the voltage dependence of the polaron-pair dissociation rate.

hexafluorophosphate as the supporting electrolyte. Silver reference, platinum counter, and glassy carbon working electrodes were used with the potentiostat.

IV. RESULTS

The RuL_3 complexes investigated, each with a different ligand, L, are shown in Fig. 3(b). Each complex was used as a 100 Å or 200 Å thick buffer layer in the OPV structure of Sec. III. Devices with a 100 Å thick buffer layer exhibited similar performance independent of composition, as shown in Fig. 4. Power conversion efficiencies range from 1.0% ± 0.3% to 1.4% ± 0.3% and are comparable to that of an analogous BCP-based device.[1] Since performance is independent of Ru-complex composition, we infer that electron transport through these thin layers occurs via trap states due to damage incurred during cathode deposition, similar to electron transport via BCP traps.

In contrast, devices with 200 Å thick buffer layers exhibit performance that is strongly dependent on buffer layer composition. Figure 5 shows the J-V characteristics for a series of RuL_3-based devices under 1 sun illumination. These same characteristics are replotted in greater detail in the semi-log plot of Fig. 6. A current inflection results in a reduction in fill factor and, concomitantly, power conversion efficiency.

We use UPS to characterize the effect of the buffer energy levels on the J-V inflection to clarify the conduction mechanisms in RuL_3.[26] Thickness-dependent UPS measurements of the HOMO and vacuum level (E_{vac}) of thin films have often shown that: (1) the Schottky-Mott limit of E_{vac} alignment across an interface is not generally valid due to the presence of an interface dipole, and (2) there can be additional E_{vac} shifts through the bulk due to built-in fields. We measured the HOMO and E_{vac} energies for 50 Å thick buffers deposited on C_{60}, with results summarized in Fig. 7(a). There is no apparent correlation between the HOMO and LUMO levels and device performance due to band bending between the buffers and C_{60} (observed as a shift in E_{vac}). However, thickness-dependent UPS data for the parent $Ru(acac)_3$ shows that most of this shift occurs over a distance of ~100 Å from the interface, and the vacuum levels at the interface are nearly that of C_{60}.[10] This suggests that the interface dipole is small so that the energy-level alignment at the A/B interface is independent of the E_{vac} shift through the bulk. In support of this conclusion, we observe a correlation between the HOMO energy and device performance by aligning the vacuum levels at the A/B interface as shown in Fig. 7(b). We find that a deeper HOMO (a larger ΔE_{HL}) results in the inflection in the J-V characteristic shifted further toward reverse bias.

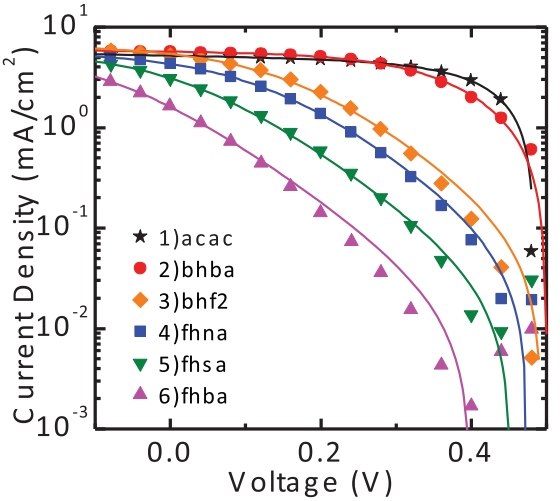

FIG. 6. (Color online) The J-V characteristics in Fig. 5 replotted on a semi-log scale. Fits to the data using model in text are shown by lines.

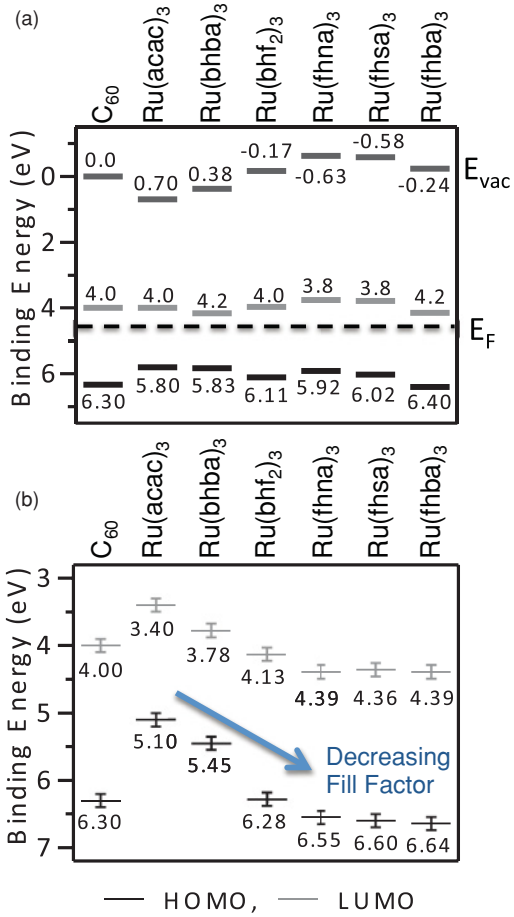

FIG. 7. (Color online) (a) Energy levels measured by a combination of ultraviolet photoelectron spectroscopy (for the highest occupied molecular orbital, HOMO) and cyclic voltammetry (for the lowest unoccupied MO, or LUMO) for 5-nm-thick RuL_3 buffer layers on C_{60} (5 nm)/ITO. (b) Energy-level alignment at the acceptor/buffer interface obtained assuming vacuum-level alignment.

V. DISCUSSION

The J-V inflection observed in these reciprocal carrier collection devices is a feature that is frequently found in OPVs, and often results from conditions used in device fabrication.[13,16] In some cases, the inflection can arise from a hole or electron transport layer with poorly matched transport levels.[14,28,29] Applying the model in Sec. II, we find Eq. (10) has the functional form to replicate the inflection as shown by the inset of Fig. 5, which is a fit to the $Ru(fhna)_3$ device data with all the parameters taken independent of voltage (solid line). This simplified expression fits the inflection but not the reverse bias slope.

The dominant source of reverse voltage dependence of the current is the PP dissociation rate, and therefore also η_d, which is described by Onsager-Braun dissociation.[21] The reverse-biased electric field lowers the barrier for separating coulombically bound PPs and increases the dissociation rate following:

$$k_{d,\mathrm{AB}} = \frac{3}{4\pi a_{\mathrm{AB}}^3} k_{\mathrm{rec,AB}} \exp\left(-\frac{E_B}{k_B T}\right)(J_1(2\sqrt{-2b})/\sqrt{-2b}), \tag{13}$$

with a similar expression for $k_{d,\mathrm{DA}}$. Here a_{AB} is the initial PP separation, $b = q^3 F_I/(8\pi\varepsilon k_B{}^2 T^2)$, E_B is the PP binding energy, F_I is the interface electric field, and J_1 is the first-order Bessel function. This model applies for fields directed from the acceptor toward the donor where it enhances charge separation—this is the case at the D/A junction when $V_a < \mathrm{V_{bi}}$. When a junction is forward biased at $V_a > \mathrm{V_{bi}}$, the field is directed from the donor toward the acceptor so that it does not enhance charge separation. As stated previously, this is the case at the reversed A/B junction when $V_a < \mathrm{V_{bi}}$, and we retain the zero field dissociation rate $k_{d,\mathrm{AB}} \approx k_{d,\mathrm{AB},0}$.

Expanding the Bessel function in (13), and assuming the interface field is linearly dependent on voltage (i.e., the current is sufficiently small to avoid space charge effects), then:

$$k_{d,\mathrm{DA}} \approx k_{d,\mathrm{DA},0}(1 - BV_a). \tag{14}$$

This rate appears explicitly in Eq. (10), and is also present in J_{sD} and J_{ph} via $\eta_{d,\mathrm{DA}}$. The large and constant reverse bias slope suggests that $\eta_{d,\mathrm{DA}}$ is small over this voltage range, such that $\eta_{d,\mathrm{DA}} \approx k_{d,\mathrm{DA}}/k_{r,\mathrm{DA}}$. Then J_{sD} is constant and the photocurrent is $J_{\mathrm{ph}} = qJ_x k_{d,\mathrm{DA},0}(1 - BV_a)/k_{r,\mathrm{DA}} = J_{\mathrm{ph},0}(1 - BV_a)$. Then (10) becomes

$$J = \left(J_{sD}\left(\exp\left(\frac{qV_a}{n_D k_B T}\right) - 1 + BV_a\right) - J_{\mathrm{ph},0}(1 - BV_a)\right) \Big/ \times \left(1 + \frac{J_{sD}}{J_{s\mathrm{AB}}} \exp\left(\frac{qV_a}{n_D k_B T}\right)\right). \tag{15}$$

These approximations account for the first-order field dependence of PP dissociation, and allow fitting the $Ru(fhna)_3$ data as shown in Figs. 5 and 6. Note that the data under forward bias do not show the saturation of the second junction, as is apparent in Fig. 2. This is attributed to forward biased breakdown of the A/B junction at $V_a \approx 0.5$V in the experimental devices.

Comparing Eq. (15) with the equivalent circuit expression of Eq. (12), we find the discrepancy between the models is due to the shunt resistance and field-dependent dissociation terms. For typical devices, the natural logarithm term in Eq. (12) is negligible, and the reverse bias slope is linear in V_a/R_p. In this case, the equivalent circuit analysis allows R_p to accurately reflect the first-order field dependence of PP dissociation, where R_p is given by:

$$R_p = 1/[(J_{\mathrm{ph},0} + J_{sD})B]. \tag{16}$$

Thus, the phenomenological equivalent circuit model converges to the physical model for back-to-back junctions in OPVs.

The J-V data can now be fit using (15) with only five parameters: n_D, J_{sD}, $\mathrm{J}_{s\mathrm{AB}}$, $J_{\mathrm{ph},0}$, and B. This is further simplified since n_D and J_{sD} depend only on the donor and acceptor and, hence, should remain independent of the buffer material, while we expect $J_{s\mathrm{AB}}$ to depend only on buffer composition. We also find that B is varied to match the reverse bias slopes of the different devices, as discussed above. In Figs. 5 and 6 we plot the J-V data (points) along with the fits (lines). For $V_a > 0.5$ V, the current grows exponentially due to breakdown of the reverse-biased A/B junction. The fitting parameters are

TABLE II. Fit results to model in text for OPVs with several different RuL_3 buffer compositions.Common Parameters: $J_{sD} = 16.0 \pm 1.5\ \mu A/cm^2$, $n_D = 3.31 \pm 0.05$.

Buffer	J_{sAB} (mA/cm^2)	$J_{ph,0}$ (mA/cm^2)	B (V^{-1})
1) $Ru(acac)_3$	9 (+100/-2)	5.2 ± 0.1	0.31 ± 0.01
2) $Ru(bhba)_3$	2.1 ± 0.2	5.7 ± 0.1	0.15 ± 0.01
3) $Ru(bhf_2)_3$	$(9.2 \pm 0.8) \times 10^{-2}$	6.3 ± 0.1	0.19 ± 0.01
4) $Ru(fhna)_3$	$(6.4 \pm 0.5) \times 10^{-2}$	5.4 ± 0.1	0.23 ± 0.02
5) $Ru(fhsa)_3$	$(2.0 \pm 0.2) \times 10^{-2}$	5.6 ± 0.1	0.14 ± 0.02
6) $Ru(fhba)_3$	$(6.4 \pm 0.8) \times 10^{-3}$	5.5 ± 0.1	0.17 ± 0.03

listed in Table II, and the errors represent a 95% confidence interval for the nonlinear regression fit. Due to the lack of *J-V* inflection, the fit only gives a lower limit to J_{sAB} for the $Ru(acac)_3$ device.

The position of the *J-V* inflection is determined by J_{sAB}, which varies over three decades for the various RuL_3 buffers studied. Now, J_{sAB} is given in Eq. (6), and we expect $p_{AB,0}$ and $\eta_{r,AB} = (1 - \eta_{d,AB}) = k_{r,AB}/(k_{r,AB} + k_{d,AB})$ to be dependent on the positions of the buffer HOMO and LUMO energies. We treat the dissociation rate, $k_{d,AB}$, as constant for all buffers since it is a function of hole mobility and dielectric constant through k_{rec} and E_B[30] in the Onsager-Braun model, which we expect to be reasonably materials independent. Hence, the current inflection is determined either by the carrier density at the A/B interface, $p_{AB,0}$, or by the recombination rate, $k_{r,AB}$.

The energies in Fig. 7(b) reveal a correlation between device performance and the HOMO position at the A/B interface. However, away from this interface [Fig. 7(a)], vacuum level shifts eliminate this consistent variation of device performance with HOMO energy. This suggests that the observed J_{sAB} trend is not dominated by variations in $p_{AB,0} \propto \exp(-(E_F - E_{HOMO,B})/k_BT)$, and we do not observe this relationship in J_{sAB}. To simplify the analysis, therefore, we assume that $p_{AB,0}$ and all the other terms in Eq. (6) are consistent across this set of devices, varying only the PP recombination rate $k_{r,AB}$.

The *J-V* inflection, therefore, occurs when $k_{r,AB} \ll k_{d,AB}$, so that $J_{sAB} \propto \eta_{r,AB} \propto k_{r,AB}$. In Fig. 8 we plot J_{sAB} vs. ΔE_{HL} and scale the right axis by typical values for the terms in Eq. (6) to represent $k_{r,AB}$. We use $a_{AB} = 1.5$ nm,[12] $\mu_A = 10^{-2}$ cm^2/Vs,[31] $\mu_B = 10^{-5}$ cm^2/Vs, $\sigma_A = 8 \times 10^{-7}$ S/cm,[32] $\sigma_B = 2 \times 10^{-7}$ S/cm,[10] $\varepsilon_A = \varepsilon_B = 3\varepsilon_0$,[12] $k_{rec,AB} = q(\mu_A + \mu_B)/\varepsilon$ for Langevin recombination,[20] $k_{d,AB} = 10^9$ s^{-1} from Eq. (13) with a PP binding energy of 0.2 eV, $p_{AB,0} = \sigma_B/q\mu_B = 10^{17}$ cm^{-3} and $n_{AB,0} = \sigma_A/q\mu_A = 10^{15}$ cm^{-3}, which are typical of trapped carrier densities that dominate the intrinsic carrier density in equilibrium conditions for disordered organic semiconductors.[33,34] These estimates yield $k_{r,AB} \approx (7 \times 10^{10}$ cm^2/As$)J_{sAB}$. This suggests that $k_{r,AB}$ ranges from 6×10^8 s^{-1} to 4×10^5 s^{-1}, which is similar to rates reported for electron transfer from donor to acceptor moieties connected by a steric spacer in solution and for solid phase Langmuir-Blodgett films of donor-acceptor dyads.[35–37]

The variation in recombination rate between the several Ru-complexes studied implies that $k_{r,AB}$ decreases approximately exponentially with increasing ΔE_{HL}. This can be understood

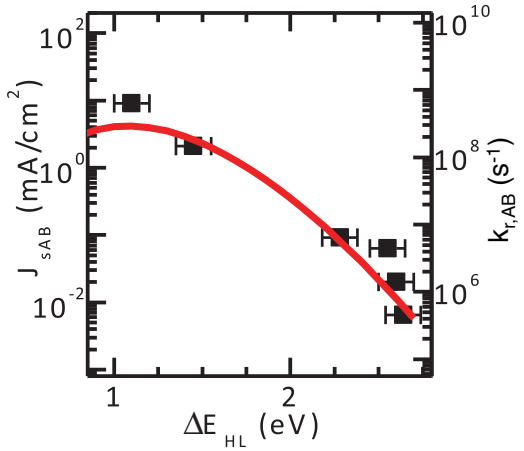

FIG. 8. (Color online) Saturation current, J_{sAB}, and polaron pair recombination rate, $k_{r,AB}$, at the acceptor/buffer layer junction compared to the interface energy gap $\Delta E_{HL} = E_{LUMO,A} - E_{HOMO,B}$ for the different buffer compositions. Here, J_{sAB} is obtained by fitting the current density vs. voltage characteristics to the model in text. $k_{r,AB}$ is estimated from J_{sAB} using (6) as described in the text.

in terms of electron transfer from the acceptor LUMO to the buffer HOMO, described by Marcus Theory in the inverted regime.[19] The electron transfer rate can be expressed as $k_{r,AB} = k_{r,AB,0} \exp(-(\lambda - \Delta E_{HL})^2/4\lambda k_B T)$ and in the inverted regime when $\Delta E_{HL} > \lambda$, the molecular reorganization energy, the rate of charge transfer is reduced exponentially with ΔE^2. However, it has been shown for organic molecules with phonon energies $> k_BT$ that the charge transfer rate can be significantly enhanced by nonadiabatic, phonon-mediated processes.[19,35,38] In this case, one must sum all high-energy phonon modes according to their Frank-Condon weighted density of states. For simplicity, we use the two parabolic potentials of Marcus Theory and consider the electron in the acceptor LUMO to be in its vibronic ground state, while we use an average vibronic energy to represent the numerous modes of the buffer molecule. In this case, the electron transfer rate is given by

$$k_{r,AB} = \sqrt{4\pi^3/h^2\ \lambda\, k_B T}|M|^2 \sum_{W=0}^{\infty} e^{-S} S^W/w! \times \exp(-(\lambda - \Delta E_{HL} + \mathrm{whv})^2/4\ \lambda\, k_B T), \quad (17)$$

where h is Plank's constant, M is the electronic coupling matrix element, $h\nu = 1500$ cm^{-1} is the average phonon energy mode chosen to represent skeletal vibrations, and S is the electron-phonon coupling strength.[35,37]

In Fig. 8, we show a fit of (17) to our measured $k_{r,AB}$ vs. ΔE_{HL} data, where $\lambda = 0.6$ eV, $S = 3.0$, and $M = 0.34$ cm^{-1}. Errors in our model parameters for calculating $k_{r,AB}$ from J_{sAB} would only result in scaling M with a square-root dependence. There are a family of curves described by Eq. (17) that fit our data within a 95% confidence interval, given by $S = 4.1$–$2.5\ \lambda$ where $\lambda = 0.1$–1.0 eV. This range is consistent with transfer rates observed in solution.[33,35] Note that J_{sAB} for the $Ru(acac)_3$ device is undefined due to the lack of an inflection; i.e. the absence of a reverse-biased characteristic suggests that J_{sAB} in this case is too large to measure. The point indicated is, therefore, a lower limit for this compound. Additionally,

while the assumption that $\eta_{r,\mathrm{AB}} = k_{r,\mathrm{AB}}/(k_{r,\mathrm{AB}} + k_{d,\mathrm{AB}}) \approx k_{r,\mathrm{AB}}/k_{d,\mathrm{AB}}$ is valid for the inflected devices with small $J_{s\mathrm{AB}}$, it is not necessarily accurate for those based on $\mathrm{Ru(acac)_3}$.

Our analysis shows that hole-transporting buffer layers can limit the current in OPVs under intense illumination. This effect can be minimized and under many practical conditions even eliminated if the HOMO-LUMO energy at the A/B interface is minimized, thereby maximizing the PP recombination rate, k_r. In the case of the $\mathrm{RuL_3}$ compounds, $\mathrm{Ru(acac)_3}$ is an optimized buffer compared to, for example, $\mathrm{Ru(fhba)_3}$, where ΔE_{HL} is increased from 1.1 eV to 2.6 eV with a corresponding decrease in k_r, which depends exponentially with $\Delta E_{\mathrm{HL}}{}^2$.

VI. CONCLUSION

In summary, we synthesized a series of *tris*(β-diketonato)ruthenium(III) analogues for use as hole transporting buffer layers. The resulting OPV *J-V* characteristics are described in terms of reciprocal carrier collection at the donor/acceptor and acceptor/buffer layer junctions. The material-independent performance observed for buffer layer thicknesses <100 Å suggests that charge transport in this case is due to damage-induced defects in the $\mathrm{RuL_3}$ complex on metal cathode deposition, similar to that observed for BCP buffers. Incorporating thicker (200 Å) films[10] leads to device characteristics that strongly depend on the composition of the buffer. Specifically, we observe an increasing *J-V* inflection for buffer materials with deeper HOMO energies.

We utilized a detail balance model to describe the observed *J-V* inflection based on free-polaron and PP recombination dynamics and compared our results to the phenomenological antipolar diode equivalent circuit model that is often applied to OPV devices that exhibit an S-shaped kink in their *J-V* characteristics. The inflection is found to depend strongly on the acceptor/buffer layer saturation current, $J_{s\mathrm{AB}}$, that leads to a barrier to charge extraction. Here, $J_{s\mathrm{AB}}$ depends on the material-dependent PP recombination rate, $k_{r,\mathrm{AB}}$, and the equilibrium hole density $p_{\mathrm{AB},0}$, at the A/B interface. While a larger buffer HOMO energy would suggest a larger injection barrier from the cathode, and therefore a reduced $p_{\mathrm{AB},0}$, our UPS data suggests the presence of vacuum level shifts that offset the variations in HOMO energies. We find that $J_{s\mathrm{AB}}$ varies by several orders of magnitude between the materials studied and is a function of the HOMO energy of the buffer and, hence, the A/B interface energy gap $\Delta E_{\mathrm{HL,AB}}$. The behavior of $J_{s\mathrm{AB}}$ is understood in terms of nonadiabatic electron transfer in the Marcus inverted regime.

Generally, we have shown that a barrier to charge extraction can dramatically reduce OPV power conversion efficiency and have demonstrated that free-polaron and PP dynamics can be used to understand and optimize the choice of buffer. For reciprocal carrier collection devices, device architectures should utilize buffer materials that provide a small ΔE_{HL} and large PP recombination efficiency to optimize power conversion efficiency.

ACKNOWLEDGMENTS

This work was funded by the US Department of Energy, Office of Science, Office of Basic Energy Sciences, through the Energy Frontier Research Centers: the Center for Energy Nanoscience at the University of Southern California (Award No. DE-SC0001013, materials synthesis, C.W.S.) and the Center for Solar and Thermal Energy Conversion in Complex Materials at the University of Michigan (Award No. DE-SC0000957, theoretical analysis, S.R.F.); the Center for Advanced Molecular Photovoltaics (Award No. KUS-C1-015-21), made by King Abdullah University of Science and Technology (KAUST, C.W.S. and M.E.T.); the collaborative R&D program with technology advanced country (2009-advanced-B-015), by the Ministry of Knowledge and Economy of Korea between Dankook University and the University of Michigan (UPS measurements, C.K.R.); and by Global Photonic Energy Corporation (materials analysis, M.E.T. and S.R.F.).

---

*C.K.R. and C.W.S. contributed equally to the results in this paper.

[1] P. Peumans, A. Yakimov, and S. R. Forrest, J. Appl. Phys. **93**, 363 (2003).
[2] P. Peumans, V. Bulovic, and S. R. Forrest, Appl. Phys. Lett. **76**, 2650 (2000).
[3] S. E. Burns, N. Pfeffer, J. Guner, M. Remmers, T. Javoreck, D. Neher, and R. H. Friend, Adv. Mater. **9**, 395 (1997).
[4] S. Yoo, W. J. Potscavage, B. Domercq, S. H. Han, T. D. Li, S. C. Jones, R. Szoszkiewicz, D. Levi, E. Riedo, S. R. Marder, and B. Kippelen, Solid-State Electron. **51**, 1367 (2007).
[5] J. Huang, J. S. Yu, H. Lin, and Y. D. Jiang, J. Appl. Phys. **105**, (2009).
[6] V. Bulovic, P. Tian, M. R. Gokhale, and S. R. Forrest, Appl. Phys. Lett. **70**, 2954 (1997).
[7] P. Peumans and S. R. Forrest, Appl. Phys. Lett. **79**, 126 (2001).
[8] Y. Hirose, A. Kahn, V. Aristov, P. Soukiassian, V. Bulovic, and S. R. Forrest, Phys. Rev. B **54**, 13748 (1996).
[9] A. Kahn, N. Koch, and W. Y. Gau, J. Polym. Sci. B **41**, 2529 (2003).
[10] B. P. Rand, J. Li, J. Xue, R. J. Holmes, M. E. Thompson, and S. R. Forrest, Adv. Mater. **17**, 2714 (2005).
[11] D. R. Eaton, J. Am. Chem. Soc. **87**, 3097 (1965).
[12] N. C. Giebink, G. P. Wiederrecht, M. R. Wasielewski, and S. R. Forrest, Phys. Rev. B **82**, 155305 (2010).
[13] M. Glatthaar, M. Riede, N. Keegan, K. Sylvester-Hvid, B. Zimmerman, M. Niggemann, A. Hinsch, and A. Gombert, Sol. Ener. Mater. Sol. Cells **91**, 390 (2007).
[14] C. C. Oey, A. B. Djurisic, H. Wang, K. K. Y. Man, W. K. Chan, M. H. Xie, Y. H. Leung, A. Pandey, J-M. Nunzi, and P. C. Chui, Nanotechnology **17**, 706 (2006).
[15] B. Kouskoussa, M. Morsli, K. Benchouk, G. Louarn, L. Cattin, A. Khelil, and J. C. Bernede, Phys. Status Solidi A **206**, N2 311 (2009).
[16] B. T. de Villers, C. J. Tassone, S. H. Tolbert, and B. J. Schwartz, J. Phys. Chem. C **113**, 18978 (2009).

[17]B. Mazhari, Sol. Ener. Mater. Sol. Cells **90**, 1021 (2006).
[18]A. Godoy, L. Cattin, L. Toumi, F. R. Diaz, M. A. del Valle, G. M. Soto, B. Kouskoussa, M. Morsli, K. Benchouk, A. Khelil, and J. C. Bernede, Sol. Ener. Mater. Sol. Cells **94**, 648 (2010).
[19]R. A. Marcus and N. Sutin, Biochim. Biophys. Acta **811**, 265 (1985).
[20]S. M. Sze, *Physics of Semiconductor Devices* (Wiley, New York, 2005).
[21]C. L. Braun, J. Chem. Phys. **80**, 4157 (1984).
[22]A. Endo, M. Kajitani, M. Mukaida, K. Shimizu, and G. P. Sato, Inorg. Chim. Acta **150**, 25 (1988).
[23]A. Endo, Y. Hoshino, K. Hirakata, Y. Takeuchi, K. Shimizu, Y. Furushim, H. Ikeuchi, and G. P. Sato, B. Chem. Soc. Jpn. **62**, 709 (1989).
[24]G. S. Patterson and R. H. Holm, Inorg. Chem. **11**, 2285 (1972).
[25]R. F. Handy and R. L. Lintvedt, Inorg. Chem. **13**, 893 (1974).
[26]See Supplemental Material at http://link.aps.org/supplemental/10.1103/PhysRevB.84.045315 for detailed UPS spectra.
[27]P. I. Djurovich, E. I. Mayo, S. R. Forrest, and M. E. Thompson, Org. Electron. **10**, 515 (2009).
[28]K. Schulze, C. Uhrich, R. Schuppel, K. Leo, M. Pfeiffer, E. Brier, E. Reinold, and P. Bauerle, Adv. Mater. **18**, 2872 (2006).
[29]H. Jin, M. Toumikoski, J. Hiltunen, P. Kopola, A. Maaninen, and F. Pino, J. Phys. Chem. C **113**, 16807 (2009).
[30]M. Pope and C. E. Swenberg, *Electronic Processes in Organic Crystals and Polymers* (Oxford University Press, New York, 1999).
[31]J. N. Haddock, X. Zhang, B. Domercq, and B. Kippelen, Org. Electron. **6**, 182 (2005).
[32]A. Hamed, Y. Y. Sun, Y. K. Tao, R. L. Meng, and P. H. Hor, Phys. Rev. B **47**, 10873 (1993).
[33]W. L. Kalb, S. Haas, C. Krellner, T. Mathis, and B. Batlogg, Phys. Rev. B **81**, 155315 (2010).
[34]A. W. Hains, Z. Liang, M. A. Woodhouse, and B. A. Gregg, Chem. Rev. **110**, 6689 (2010).
[35]G. L. Closs, L. T. Calcaterra, N. J. Green, K. W. Penfield, and J. R. Miller, J. Phys. Chem. **90**, 3673 (1986).
[36]H. Lemmetyinen, N. V. Tkachenko, A. Efimov, and M. Niemi, Phys. Chem. Chem. Phys. **13**, 397 (2011).
[37]J. E. Moser and M. Gratzel, Chem. Phys. **176**, 493 (1993).
[38]R. P. Van Duyne and S. F. Fischer, Chem. Phys. **5**, 183 (1974).